

# Non-centered inversion symmetry in momentum space

Bin-Bin Liu,<sup>1,\*</sup> Xian-Lei Sheng,<sup>1,2,†</sup> Y. X. Zhao,<sup>3,4,‡</sup> and Shengyuan A. Yang<sup>5,6</sup>

<sup>1</sup>*School of Physics, Beihang University, Beijing 100191, China*

<sup>2</sup>*Peng Huanwu Collaborative Center for Research and Education, Beihang University, Beijing 100191, China*

<sup>3</sup>*National Laboratory of Solid State Microstructures and Department of Physics, Nanjing University, Nanjing 210093, China*

<sup>4</sup>*Collaborative Innovation Center of Advanced Microstructures, Nanjing University, Nanjing 210093, China*

<sup>5</sup>*Research Laboratory for Quantum Materials, Singapore University of Technology and Design, Singapore 487372, Singapore*

<sup>6</sup>*Center for Quantum Transport and Thermal Energy Science,  
School of Physics and Technology, Nanjing Normal University, Nanjing 210023, China*

Symmetry is prevalent in physics, where the spacial inversion symmetry is one of the most important symmetries which defines the parity. It inverses the real space position as well as the momentum of a physical system relative to the original point in the real and momentum spaces. Here, we discover a new kind of inversion symmetry which inverses the real space position relative to the origin but is non-centered in the momentum space. We derive the momentum-non-centered inversion symmetry with projectively enriched symmetry algebras and demonstrate it in Hamiltonians in  $\pi$ flux lattices in both 2D and 3D. Intriguingly, we discover Mobius insulators with shifted-inverse edge states at half-fillings and a high Chern number insulator that has off-centered chiral edge states at quarter-fillings, which have not been reported before. We also define quantized topological numbers that indicate the existence of the novel edge states with off-centered crossing points in the momentum space. We design topological circuits that correspond to our Hamiltonian and perform simulations, which agree with our theoretical predictions. Our findings suggest new routes for exploring topological edge responses with projective symmetries in artificial systems.

Symmetry is paramount in physics. The inversion symmetry plays a vital role in determining the parity of a system and classification of topological states. While the inversion symmetry is well understood, its projective representation and how it modifies the momentum space actions, however, are barely explored. Here, we propose novel momentum nonsymmorphic inversion symmetries that have additional translations of *half* reciprocal lattice translations in the momentum space and explore its unique physical consequences in lattice models and artificial systems.

Due to a half glide of reciprocal lattice vector in the momentum space, the inversion center are shifted by a *quarter* of reciprocal lattice vector. We call it momentum-non-centered inversion symmetry (MNCIS). We propose and investigate both 2D and 3D MNCIS with inversion centers at  $(n\pi, \pm\pi/2)$  [or  $(\pm\pi/2, n\pi)$ ],  $(\pm\pi/2, \pm\pi/2)$ , and  $(\pm\pi/2, \pm\pi/2, \pm\pi/2)$  ( $n, n' = 0, \pm 1$ ), which are distinct from the conventional inversion centers at time-reversal invariant (TRIM) points.

Gauge field is proved of great importance to topological states of matter[1–4]. Among all the flux's values,  $\pi$ -flux preserves time-reversal symmetry and is valued in  $\mathbb{Z}_2$ , which has potential to modify the symmetry algebras by switching the commutation into anti-commutation relation and vice versa[5–7]. We construct lattice models with  $\mathbb{Z}_2$  gauge fields to realize the MNCIS.

There are two special aspects about the MNCIS. One is that the real and momentum inversion centers

are not coincides; the other is that the momentum inversion centers and the TRIM points are not coincides. Exploring the first aspect, we find that the MNCIS is essential in determining the behavior of the edge/surface states. Distinct from the edge states related by normal inversion symmetry, those related by the MNCIS have non-centered fixed points in a reduced Brillouin subspace. With this observation, we discover Mobius insulators with shifted-inverse edge states at half-fillings and a Chern insulator with a high Chern number  $c_n = 2$  that has off-centered chiral edge states at quarter-fillings, which have not been reported before. The second aspect, the mismatch between TRIM points and inversion centers, lead to dramatic topological consequences. The key is that the time-reversal symmetry determines which pair of inversion centers are equivalent and band inversions are the same at equivalent centers. As a consequence, in 2D, for example, systems with inversion centers at  $(\pm\pi/2, \pm\pi/2)$  has topological edge states along both edge directions, while systems with  $(n\pi, \pm\pi/2)$  has only topological edge states along y-edge. In 3D, systems with inversion centers at  $(\pm\pi/2, \pm\pi/2, \pm\pi/2)$  can feature 2D BZ slices of nontrivial Chern numbers, which can be used to determine the existence of Weyl points.

We define quantized topological indicators of  $\mathbb{Z}_2$  classification to characterize the novel edge spectra and provide formulas to calculate it. It is originated from a guaranteed Berry phase  $\theta = \pi$  obtained by integrating Berry connections along an 1D-subspace in the BZ across two adjacent non-centered inversion centers, which can either be read from Wilson loop spectra or from parity of the two centers.

We provide a general way of designing topological circuits to realize our lattice models and give simulation

---

\* bblu@buaa.edu.cn

† xlsheng@buaa.edu.cn

‡ zhaoyx@nju.edu.cn

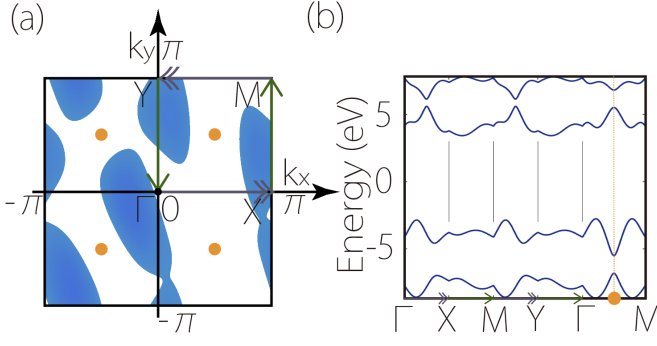


FIG. 1. (a) Energy spectra of the  $H_{xy}^{2D}$  in the first BZ with a constant energy cut-off. Centers of the MNCIS are noted as orange dots. Arrows with same colors (or shapes) are equivalent. (b) The energy spectra along high-symmetry lines in the first BZ.

results that are in good agreement with the theoretical predictions. Our setup provide a guidance for further experimental realizations in circuits. The model and theory can also be readily realized and tested in other artificial systems where adding the  $\mathbb{Z}_2$  gauge fields preserving time-reversal symmetry are possible.

*Momentum-non-centered inversion symmetry (MNCIS).*— Contrary to the conventional inversion symmetry, the momentum-non-centered inversion symmetry we propose is non-symmorphic and has additional translation of half reciprocal lattice vectors,  $\mathcal{P}\mathcal{L}_{G/2}$ , where the G stands for reciprocal lattice vector. The  $P$  is a normal inversion symmetry with the form

$$P = U\hat{I} \quad (1)$$

where the  $U$  acts on the real space's orbital/pseudo-spin and  $\hat{I}$  on the momentum. The Hamiltonian  $H$  that possesses the  $P$ , i.e  $PH P^\dagger = H$  leads to

$$UH(-\mathbf{k})U^\dagger = H(\mathbf{k}). \quad (2)$$

To realize the momentum glide, we introduce the following algebra  $\{P, L_i\} = 0$ . It follows that

$$PL_i P^\dagger = -L_i^{-1} = e^{i(k_i + G_i/2)a_i} \quad (3)$$

with  $a_i$  lattice vectors and  $i=x,y,z$ . This implies that the inversion is projectively enriched by glide of half reciprocal lattice  $G_i/2$  along  $k_i$ , which yields the MNCIS:

$$\mathcal{P}_i = P\mathcal{L}_{G_i/2} \quad (4)$$

To see the how the  $\mathcal{P}$  becomes non-centered, we investigate a 2D Hamiltonian  $H_y^{2D}$  obeying the  $\mathcal{P}_y$  as an example and get

$$U_{2D}H_y^{2D}(-k_x, -k_y + \pi)U_{2D}^\dagger = H_y^{2D}(k_x, k_y). \quad (5)$$

As a result, the inversion centers of the  $\mathcal{P}_y^{2D}$  are shifted a *quarter* of reciprocal lattice vector  $G_y$  along  $k_y$  and

becomes  $(n\pi, \pm\pi/2)$  ( $n = 0, \pm 1$ ). Note that the real space inversion centers stay still— $(na/2, n'b/2)$ —which are centered in the unite cell.

The momentum glides can be added freely in different directions. Apart from  $\{P, L_y\} = 0$ , if we further implement  $\{P, L_x\} = 0$ , it leads to

$$\mathcal{P}_{xy}^{2D} = U^{2D}\mathcal{L}_{G_x/2}\mathcal{L}_{G_y/2}\hat{I}_{xy} \quad (6)$$

A Hamiltonian that obeys Eq. (6) gives rise to

$$UH_{xy}^{2D}(-k_x + \pi, -k_y + \pi)U^\dagger = H_{xy}^{2D}(k_x, k_y). \quad (7)$$

The  $\mathcal{P}_{xy}$  has inversion centers at  $(\pm\pi/2, \pm\pi/2)$ . It can even be extended in 3D as

$$\mathcal{P}_{xyz}^{3D} = U_{3D}\mathcal{L}_{G_x/2}\mathcal{L}_{G_y/2}\mathcal{L}_{G_z/2}\hat{I}_{xyz} \quad (8)$$

which characterizes

$$U_{3D}H_{xyz}^{3D}(-k_x + \pi, -k_y + \pi, -k_z + \pi)U_{3D}^\dagger = H_{xyz}^{3D}(k_x, k_y, k_z). \quad (9)$$

Next, we demonstrate these MNCISs in physical systems and reveal their physical consequences.

*Physical Realizations of MNCISs in 2D and 3D models.*— The key to realizing the MNCIS  $\mathcal{P}$  is to have projective symmetry algebras. In tight-binding conventions, the additional  $\pi$ -phase required by the anti-symmetric symmetry algebras can be achieved through negative topplings. We apply the  $\mathbb{Z}_2$  gauge fields on  $\pi$ -flux lattices to construct our models.

To realize a Hamiltonian with  $\mathcal{P}_{xy}^{2D}$ , we construct a lattice model as shown in Fig. 2 (a). All red bonds are attached with a  $\pi$  phase and hence are minus, as  $e^{i\pi} = -1$ . The bond width indicates the magnitude. In the unite cell convention, the inversion operation flips the gauge configuration (i.e., the position of the red bonds), but preserves the dimerization pattern and the flux configuration. The anti-commutation  $\{P, L_i\} = 0$  comes from a  $\pi$  phase acquired by the  $L_i$  following a closed path by  $PL_iP^{-1}L_i^{-1}$ , which is evidenced from the Fig. 2 (a). We break the time-reversal symmetry, which is centered at TRIM points, to demonstrate the our model construction. The spectra of the model is show in Fig. 1 (a), where the inversion centers are in each quadrants of the BZ. Following the prescription, we can also construct a model for the  $\mathcal{P}_y^{2D}$  as shown in Fig. 3 (a). The resulting Hamiltonian  $H_y^{2D}$  possesses the momentum non-centered inversions as shown in Fig. 3 (a).

One prominent consequence of the MNCIS lies in its modification on the edge spectra. For a 2D slab geometry with periodic  $i$  ( $k_i$ ), the MNCIS is projected as

$$\mathcal{P}_i^{slab} = U_{2D}^{slab}\mathcal{L}_{G_i/2}\hat{I}_i \quad (10)$$

where the  $U_{2D}^{slab}$  is the real space inversion operation of the orbitals of the slab. This means that the two edges of the slab related by  $U_{slab}$  may characterize states that are related by a non-centered inversion in  $k_y$  subspace,

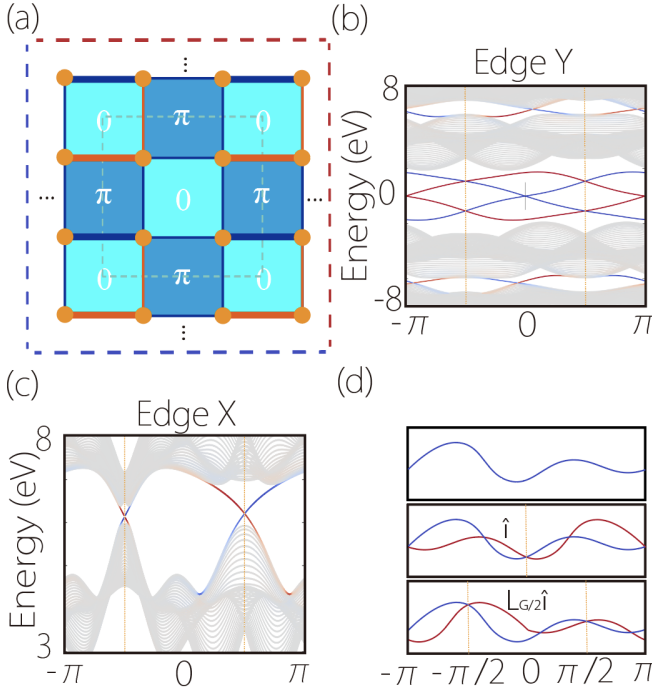


FIG. 2. Lattice model and spectra with the  $\mathcal{P}_{xy}^{2D}$  symmetry. (a) 2D lattice model with gauge distributions and dimerization patterns specified. Each red bond is attached with a  $\pi$  flux as  $e^{i\pi} = -1$ . The flux through each plaquette is determined by the number of red bond forming it. The bond width indicates the magnitude of the bond. The unit cell is outlined with gray dashed square. (b) and (c) are edge states along Y and X edges specified in (a), with colors (red and blue) indicating the location of the edges. The edge states preserve Eq. (11). The model features Mobius insulators with shifted-inverse edge states at half-fillings and a Chern insulator with a high Chern number  $c_n = 2$  that has off-centered chiral edge states at quarter-fillings, which have not been reported before. (d) Schematic plot for the edge states related by non-centered inversion symmetry in a 1D slab and the comparison with the centered chiral edge states, where  $\hat{I}$  and  $\hat{\mathcal{L}}_{G/2}$  are momentum space inversion and translation of half reciprocal lattice vector.

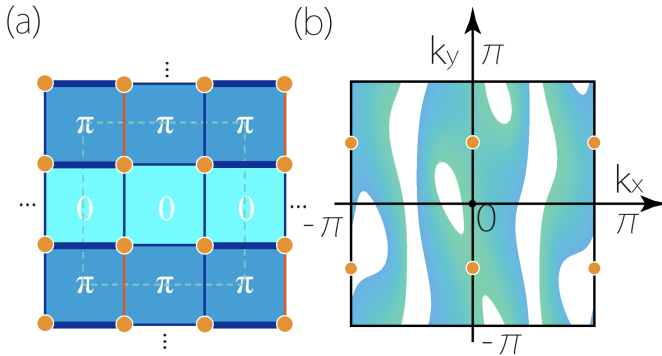


FIG. 3. Lattice model and spectra with the  $\mathcal{P}_y^{2D}$  symmetry. (a) The lattice model. (b) The band structure in the first BZ with an energy cut-off. The dots are inversion centers which line both in and on the boundary of the BZ.

distinct from the edge states related by normal inversion symmetry, as shown in the Fig. 2 (d), where the dashed lines show a shift in 1D inversion/reflection centers.

This observation explains the edge spectra in Fig. 2 (b) (c), where the blue and red lines are the states localized at opposite edges [Fig. 3 (a)]. The combination of the states from two edges has fixed points at  $\pm\pi/2$  in the reduced BZ. Intriguingly, our model for the  $H_{xy}^{2D}$  features Mobius insulators with shifted-inverse edge states at half-fillings and a Chern insulator with a high Chern number,  $c_n = 2$ , that has off-centered chiral edge states at quarter-fillings, which have not been reported before.

The topological edge states here are stable, since addition of trivial atomic bands does not affect the nontrivial topological edge states, which can be described in K-theoretical approach.

This construction methodology can be extended to 3D. In order to have inversion symmetry that is off-center in three axial directions,  $\mathcal{P}_{xyz}^{3D}$ , additional  $\mathbb{Z}_2$  gauge fields are needed in the third axis. We demonstrate this idea in a 3D lattice model in Fig. 4. It has eight orbits per unit cell, and every slice of it features a strip pattern of  $\pi$  flux. The model obeys Eq. (9) and has MNCIS defined in the Eq. (8). As a consequence, the surface states formed by two opposite surface has non-centered fixed points, as shown in Fig. 4 (d), which is a generalization of Fig. 2 (d).

$$\mathcal{P}_{ij}^{slab} = U_{3D}^{slab} \mathcal{L}_{G_i/2} L_{G_j/2} \hat{I}_{ij} \quad (11)$$

where the  $U_{3D}^{slab}$  is the real space inversion operation of the orbitals of the slab. With similar way, one can extend to construct the model with MNCIS to any higher dimensions.

Fig. 4 (c) shows one possible configuration of inversion eigenvalue (+/-) for a particular band. The Chern number on the three grey planes are all nontrivial and equals to one due to the mismatch between the inversion plane and the TRIM. Since the plane that across the TRIM points must have trivial Chern numbers, this nontrivial Chern planes indicates the existence of Weyl semimetal.

To realize other 3D MNCISs one may Stack the 2D models for  $H_{xy}^{2D}$  (or  $H_y^{2D}$ ) with no z flux and respecting the inversion symmetry. See Fig. 5 (e) in the SM.

*Topological indicators for shifted-inverse edge states.*— To characterize the topology, we investigate a well-defined vector space over a loop bundle on the Brillouin manifold around an inversion center. We formulate expression for a topological indicator defined on a quarter of BZ an inversion center.

A square BZ can be divided into four parts with respect of the four inversion centers. Each quadrant is dubbed as  $\tau_i$  with  $i = a, b, c, d$ . See Fig. 5 (a) (b). With such segmentation, each quarter can give rise to a quantized topological number. Applying the Stokes' theorem, we have  $\int_{\tau_i} \mathcal{F}(\mathbf{k}) d^2\mathbf{k} - \int_{\partial\tau_i} \mathcal{A}(\mathbf{k}) d\mathbf{k} = 0$ , with  $\mathcal{F}(\mathbf{k})$  and  $\mathcal{A}(\mathbf{k})$  the Berry curvature and Berry phase

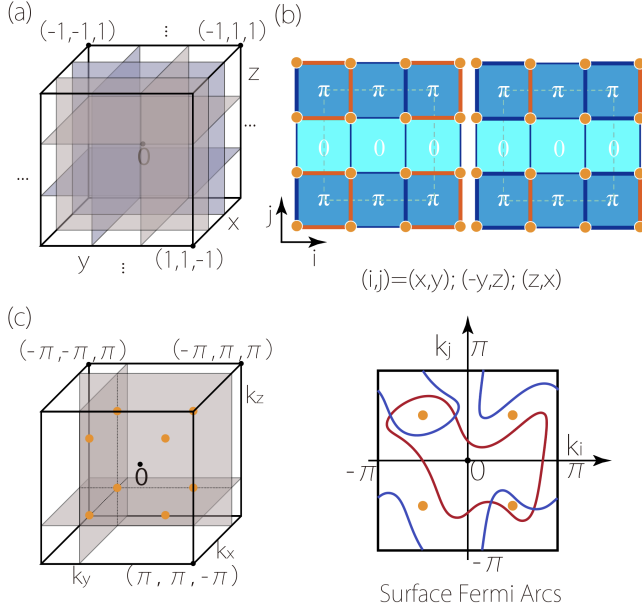


FIG. 4. 3D model with the  $\mathcal{P}_{xyz}^{3D}$  symmetry. (a) The 3D model in the real space is made of two kinds of 2D slices. Each of the dark blue slices is made of the 2D lattice in the left part of the (b); each of the lighter slices is represented by the 2D lattice in the right part of the (b). The 3D model has 8 sites per unite cell and is extended in three spacial dimensions. (c) The illustration of MNCIS with inversion center at  $(\pm\pi/2, \pm\pi/2, \pm\pi/2)$  corresponding to the model in (a). The red dots are the centers with  $\pm$  sign showing one possible configuration of inversion eigenvalue for a particular band. The Chern number on the three grey planes are all nontrivial and equals to one due to the mismatch between the inversion plane and the TRIM. (d) illustrates the surface Fermi arcs of a 3D model with the MNCIS, which have reduced MNCIS and can be viewed as extension of Fig. 2 (d).

defined for isolated and continuous bands. Here both the systems have four isolated bands, where the first and third (second and forth) bands defines sub-spaces. The following topological invariants are defined for the sub-vector spaces, i.e.,  $V(\mathbf{k}) = \text{span}[\psi_n(\mathbf{k})]$  ( $n = 1$  or  $2$ ).

Take  $H_{xy}^{2D}$  as an example. The boundary of each  $\tau_i$  is composed of four parts: right (R), up (U), left (L), down (D). Due to the equivalence of diagonal points, e.g.,  $(0,0)$  and  $(\pi,\pi)$  or  $(0,-\pi/2)$  and  $(\pi,\pi/2)$ , the D+R forms a closed loop on which the loop boundle defines a berry phase  $\gamma(D+R)$ . Restricted by the non-orientable edge connections, the  $\gamma(U+L)$  is nothing but  $\gamma(D+R)$ . Therefore, we define a topological indicator for each  $\tau_i$  as

$$u_i = \frac{1}{2\pi} \int_{\tau_i} \mathcal{F}(\mathbf{k}) d^2\mathbf{k} - \frac{1}{\pi} \gamma(D+R) \mod 2. \quad (12)$$

In the nontrivial case with  $(\pm\pi/2, \pm\pi/2)$ , we obtain  $u_a = u_d = 0$  and  $u_b = u_c = 1$ . In the nontrivial case with  $(n\pi, \pm\pi/2)$ , we find  $u_a = u_c = 0$  and  $u_b = 1, u_d = 1$ . See Fig. 5 (a) (b). In the trivial cases, all  $u_i = 0$ .

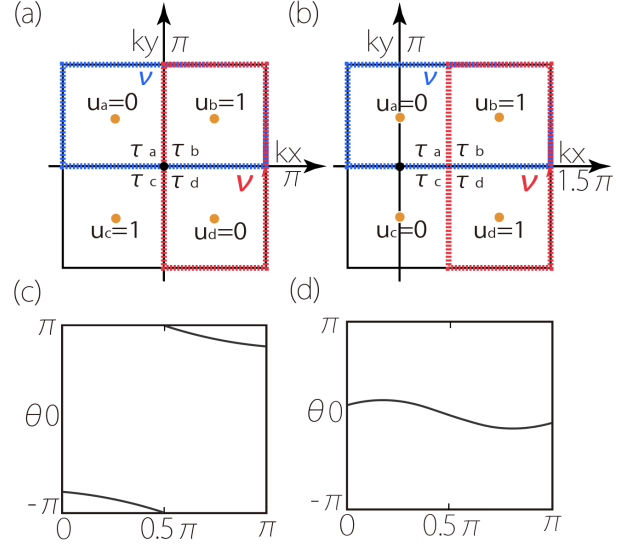


FIG. 5. Topological indicators  $u_i$  and the Wilson loop. The distribution of  $u_i$  for (a) the  $H_{xy}^{2D}$  and (b) the  $H_y^{2D}$ . The  $\nu$  ( $\nu'$ ) defined on the union of two adjacent quadrants is a  $\mathcal{Z}$  invariant, which can be read from the Wilson loop—(c) for nontrivial and (d) for trivial  $\nu$  ( $\nu'$ ). In the nontrivial case, it is guaranteed that a Berry phase  $\theta = \pi$  occurs when integrated on a line across two non-centered inversion centers.

To give a geometric apprehension, we take the union of two adjacent quadrants, e.g.,  $\tau_a \cup \tau_b$  on which the Wilson loop can be calculated. Adding  $u_a$  and  $u_b$ , we can define

$$\begin{aligned} \nu &= u_a + u_b \mod 2 \\ &= \frac{1}{2\pi} \int_{\tau_a \cup \tau_b} \mathcal{F}(\mathbf{k}) d^2\mathbf{k} - \frac{1}{\pi} \gamma(k_y = 0) \mod 2 \end{aligned} \quad (13)$$

Similarly, we can define

$$\begin{aligned} \nu' &= u_b + u_d \mod 2 \\ &= \frac{1}{2\pi} \int_{\tau_b \cup \tau_d} \mathcal{F}(\mathbf{k}) d^2\mathbf{k} + \frac{1}{\pi} \gamma(k_x = 0) \mod 2 \end{aligned} \quad (14)$$

We emphasise that the second terms of  $\nu$  and  $\nu'$  are different in a sign. The above Eq. (13) and Eq. (14) can be read off from Wilson loop. Take  $\nu'$  as an example. Since  $\int_{\tau_b \cup \tau_d} \mathcal{F}(\mathbf{k}) d^2\mathbf{k} = \gamma(k_x = \pi) - \gamma(k_x = 0)$ , we then have

$$\begin{aligned} \nu'(\nu) &= \frac{1}{2\pi} [\gamma(0) + \gamma(\pi)] \mod 2 \\ &= \zeta \mod 2 \end{aligned} \quad (15)$$

where the  $\zeta$  is a geometric quantity that counts the times of crossings of the Wilson loop spectrum with the  $\theta = \pi$  line. Therefore, we can infer the information of edge states from the  $u_i$ , such as the existence of edge states along certain edges.

We can further formulate the  $u_i$  to relate the parity



eigenvalue  $\lambda_i$  at the inversion center  $\Gamma_j$ ,

$$(-1)^{u_a+u_b} = (-1)^\nu = \prod_{j=a,b} \prod_i^N \lambda_i(\Gamma_j) \quad (16)$$

and similarly,

$$(-1)^{u_b+u_d} = (-1)^{\nu'} = \prod_{j=b,d} \prod_i^N \lambda_i(\Gamma_j) \quad (17)$$

The  $\Gamma_j$  are the inversion centers in the  $\tau_j$  quadrants of the BZ. Different from the previous  $\mathbb{Z}_2$  number, the  $\Gamma_j$  do not coincide with the time-reversal invariant momenta, but are nonsymorphic, such that  $\Gamma_j = (\pm\pi/2, \pm\pi/2)$ . In our examples, the occupation number of the sub system is  $N = 1$ . The detailed derivations are presented in the SM C. The off-centered parity eigenvalues of our models are in SMB.

Different inversion centers relative to the TRIM points lead to different topological consequences. For the  $(n\pi, \pm\pi/2)$  case, it admits topological classification by  $\nu$  in Eq. (13), which features edge state only along y. The situation is different for the  $(\pm\pi/2, \pm\pi/2)$  case, as it features another topological invariant  $\nu'$  in the nontrivial case. Therefore, not only the y edges [Fig. 2 (b)] but also the x edges [Fig. 2 (c)] host topological states.

The edge states we discussed here are stable topological, which are robust against adding trivial bands, as they are described within the K-theory.

*Experimental realizations of MNCIS*—Enjoying the development of artificial systems, the MNCIS can find experimental realizations and applications in cold atoms, optical lattices, circuits, phonons and meta-materials. Based on our TB models, we demonstrate this idea in topological circuits. We find very components of the TB models their circuits correspondences, see Fig. 10 in the SM, and hence map the Hamiltonian into a circuits' Laplacian obtained by Kirchhoff's node-current law[8].

In topological circuit, the square-root of the positive energy is mapped to the frequency of circuit,  $\omega \sim \sqrt{E_{shifted}}$ , where the  $E_{shifted}$  are the eigenvalues shifted all to positive. As an example, we simulate the  $H_{xy}^{2D}$  in the Fig. 2 (a) in a circuit device of  $21 \times 21$  unites with periodic and open boundary conditions in two directions.

The simulation results are shown in Fig. 6, which shows the non-centered chirality of the edges states. Notably, the simulation results (light dots) are in perfect agreement with theoretical predictions (thin dashed lines), which demonstrates the validity of our circuit setups and paves the way for experiments.

*Conclusion and discussion*— In conclusion, with modified symmetry algebras, we discover a new kind of inversion symmetry which inverses the real space position relative to the origin but is non-centered in the momentum space. We derive this non-centered momentum with projectively enriched symmetry algebras. We demonstrate the idea in Hamiltonians on

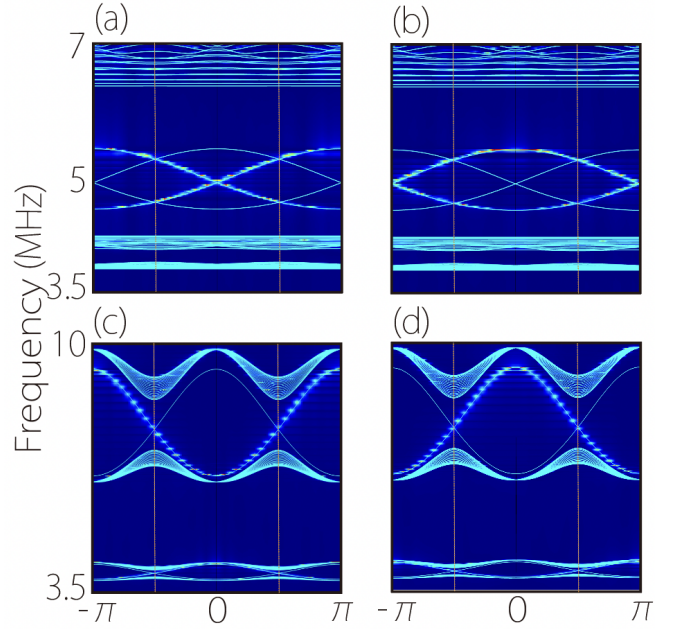


FIG. 6. Circuits' simulation results for the lattice TB model with the  $\mathcal{P}_{xy}^{2D}$  symmetry in the Fig.2. The bright yellow dots are the simulation results which are in agreement with the theoretical predictions (cyan lines). The edge states for the left (a), right (b), bottom (c) and top (d) edges are presented, which satisfy the non-centered inversion symmetry for slab geometries with the convention in the Fig.2 (a). The spectra are rescaled with relations in Eq. (E6).

flux lattices with  $\mathbb{Z}_2$  gauge field, which naturally realize the non-centered momentum inversion symmetries. We also discover unconventional  $\mathbb{Z}_2$  topological indicators emergent from the gauge fields, which are protected by the momentum-non-centered symmetries. The topological numbers  $\nu$  and  $\nu'$  can be read off from Wilson loops evolving along both reciprocal lattice vectors. We further map We find that non-trivial topological indicators defined along both vectors signal a novel topological insulator, with both of its x and y edges (four edges) hosting edge states linked by a reduced non-centered inversion symmetry in each pairs, drastically distinct from previous topological insulators.

We propose a circuits setup for our model and provide simulation results that are in good agreement with the theories' predictions. Our setup provide a guidance for further experimental realizations in circuits. The model and theory can also be readily realized and tested in other artificial systems where adding the  $\mathbb{Z}_2$  gauge fields preserving time-reversal symmetry are possible.

Our theory opens new routes for exploring physical and topological consequences associated with the momentum-non-centered inversion symmetries. We give an example on how to use the  $u_i$  to detect the oddity of Chern number. See SM E. The next theoretical pursuits would be to explore non-centered  $\mathcal{PT}$  symmetry and its topological classification, which we briefly discussed in

the SM.

## ACKNOWLEDGMENTS

We thank Rui Yu and D. L. Deng for helpful discussions. We acknowledge the computational support

from HPC of the Beihang University and Texas Advanced Computing Center. This work is supported by National Key R & D Program of China (2022YFA1402600), the NSFC (Grants No. 12174018, No. 12074024), the Fundamental Research Funds for the Central Universities, and the Singapore Ministry of Education AcRF Tier 2 (T2EP50220-0026).

- 
- [1] F. D. M. Haldane, *Phys. Rev. Lett.* **61**, 2015 (1988).
  - [2] C. L. Kane and E. J. Mele, *Phys. Rev. Lett.* **95**, 146802 (2005).
  - [3] B. A. Bernevig, T. L. Hughes, and S.-C. Zhang, *Science* **314**, 1757 (2006), <https://www.science.org/doi/pdf/10.1126/science.1133734>.
  - [4] X.-L. Qi, Y.-S. Wu, and S.-C. Zhang, *Phys. Rev. B* **74**, 085308 (2006).
  - [5] Y. X. Zhao, Y.-X. Huang, and S. A. Yang, *Phys. Rev. B* **102**, 161117 (2020).
  - [6] Y. X. Zhao, C. Chen, X.-L. Sheng, and S. A. Yang, *Phys. Rev. Lett.* **126**, 196402 (2021).
  - [7] Z. Y. Chen, S. A. Yang, and Y. X. Zhao, *Nature Communications* **13**, 2215 (2022).
  - [8] S. Imhof, C. Berger, F. Bayer, J. Brehm, L. W. Molenkamp, T. Kiessling, F. Schindler, C. H. Lee, M. Greiter, T. Neupert, *et al.*, *Nature Physics* **14**, 925 (2018).
  - [9] L. Fu and C. L. Kane, *Phys. Rev. B* **76**, 045302 (2007).
  - [10] R. Yu, Y. X. Zhao, and A. P. Schnyder, *National Science Review* **7**, 1288 (2020), <https://academic.oup.com/nsr/article-pdf/7/8/1288/38882379/nwaa065.pdf>.